

带格式的: 编号方式: 连续

# The Different Dynamic Influences of Typhoon Kalmaegi on two Pre-existing Anticyclonic Ocean Eddies

Yihao He<sup>1</sup>, Xiayan Lin<sup>1,2,\*</sup>, Guoqing Han<sup>1</sup>, Yu Liu<sup>1,3</sup> and Han Zhang<sup>2,3,\*</sup>

<sup>1</sup> Marine Science and Technology College, Zhejiang Ocean University, Zhoushan 316022, China;

<sup>2</sup> State Key Laboratory of Satellite Ocean Environment Dynamics, Second Institute of Oceanography, Ministry of Natural Resources, Hangzhou 310012, China;

<sup>3</sup> Southern Marine Science and Engineering Guangdong Laboratory (Zhuhai), Zhuhai 519082, China

\*Correspondence: Xiayan Lin (linxiayan@zjou.edu.cn) and Han Zhang (zhanghan@sio.org.cn)

**Abstract:** Using multi-source observational data and GLORYS12V1 reanalysis data, we conduct a comparative analysis of different responses of two warm eddies, AE1 and AE2 in the northern South China Sea to Typhoon Kalmaegi during September 2014. The findings of our research are as follows: (1) For horizontal distribution, the area and the sea surface temperature (SST) of AE1 and AE2 decrease by about 31% (36%) and 0.4 °C (0.6 °C). The amplitude, Rossby number ( $R_o$ =relative vorticity/Coriolis parameter) and eddy kinetic energy (EKE) of AE1 increases by 1.3 cm (5.7%),  $1.4 \times 10^{-2}$  (20.6%) and  $107.2 \text{ cm}^2 \text{ s}^{-2}$  (49.2%) after the typhoon, respectively, while AE2 weakens and the amplitude, Rossby number and EKE decreased by 3.1 cm (14.6%),  $1.6 \times 10^{-2}$  (26.2%) and  $38.5 \text{ cm}^2 \text{ s}^{-2}$  (20.2%), respectively. (2) In vertical direction, AE1 demonstrates enhanced convergence, leading to an increase in temperature and a decrease in salinity above 150 m. The response below the mixing layer depth (MLD) is particularly prominent (1.3 °C). In contrast, AE2 experiences cooling and a decrease in salinity above the MLD. Below the MLD, it exhibits a subsurface temperature drop and salinity increase due to the upwelling of cold water induced by the suction effect of the typhoon. (3) The disparity in the responses of the two warm eddies can be attributed to their different positions relative to Typhoon Kalmaegi. Under the influence of negative wind stress curl outside the maximum wind radius ( $R_{max}$ ) of typhoon triggering negative Ekman pumping velocity (EPV) and quasi-geostrophic adjustment of eddy, warm eddy AE1, with its center to the left of the typhoon's path, further enhances the converging sinking of the upper warm water, resulting in its intensification. On the other hand, warm eddy AE2, situated closer to the center of the typhoon, weakens due to the cold suction caused by the strong positive wind stress curl within the typhoon's  $R_{max}$ . Same polarity eddies may have different response to typhoons. The distance between eddies and typhoons, eddies intensity and the background field need to be considered.

删除了:  $\text{cm}^2$

删除了:  $\text{cm}^2$

删除了: Warm

删除了: locates on

删除了:

删除了: side

删除了: , experiences a positive work effect as the typhoon passed by. The negative wind stress curl in AE1 triggers a negative Ekman pumping velocity (EPV)

删除了: (?) by

删除了: thereby strengthening AE1

删除了: situates

删除了: in

删除了: center

删除了: ,

删除了: t

47 **1. Introduction**

48 Tropical cyclones (TCs), as they traverse the vast ocean, interact with oceanic mesoscale processes,  
49 particularly with mesoscale eddies, representing a crucial aspect of air-sea interaction (Shay and Jaimes,  
50 2010; Lu et al., 2016; Song et al., 2018; Ning et al., 2019; Sun et al., 2023). The South China Sea (SCS)  
51 experiences an average of six TCs passing through each year (Wang et al., 2007), causing prominent  
52 exchange of energy and mass between air and sea (Price, 1981). Meanwhile, due to the influence of the  
53 Asian monsoon, intrusion of the Kuroshio Current, and complex topography, the Northern South China  
54 Sea (NSCS) also encounters frequent eddy activities (Xiu et al., 2010; Chen et al., 2011). These  
55 mesoscale oceanic eddies often play significant roles in mass and heat transport and air-sea interaction.  
56 This unique setting offers an exceptional opportunity to investigate the generation, evolution, and  
57 termination of mesoscale eddies and their interaction with TCs.

58 Pre-existing mesoscale eddies play a crucial role in the feedback mechanism between the ocean and  
59 TCs. Cyclonic eddies (cold eddies) enhance the sea surface cooling effect under TCs conditions, resulting  
60 in TCs weakening, due to their thermodynamic structures and cold-water entrainment processes that  
61 reduce the heat transfer from the sea surface to the TCs through air-sea interaction (Ma et al., 2017; Yu  
62 et al., 2021). In contrast, anticyclonic eddies (warm eddies) suppress this cooling effect, leading to TCs  
63 intensification (Shay et al., 2000; Walker et al., 2005; Lin et al., 2011; Wang et al., 2018). Warm eddies  
64 have a thicker upper mixed layer, which stores more heat. When a TC passes over a warm eddy, it  
65 increases sensible heat and water vapor in TC's center, which are closely related to the TC's  
66 intensification (Wada and Usui, 2010; Huang et al., 2022). Furthermore, the downwelling within warm  
67 eddies hinders the upwelling of cold water, reducing the apparent sea surface cooling caused by the TCs.  
68 These processes weaken the oceanic negative feedback effect and help to sustain or even strengthen TC's  
69 development.

70 On the other hand, TCs also have a notable impact on the intensity, size, and movement of mesoscale  
71 eddies. In some cases, TCs strengthen cold eddies and can even lead to the formation of new cyclonic  
72 eddies in certain situations (Sun et al., 2014), while TCs accelerate the dissipation of anticyclonic eddies  
73 (Zhang et al., 2020). The strengthening effect of TCs on cold eddies is related to the positions between  
74 cold eddies and TCs, the intensity of eddies, and TC-induced geostrophic response (Lu et al., 2016; Yu  
75 et al., 2019; Lu et al., 2023). Cyclonic eddies on the left side of the TC's track were more intensely

删除了:

删除了: interface

删除了: ation

删除了: On one hand, from a thermodynamic perspective, TCs derive their development and sustenance energy from the ocean.

删除了: through

删除了: While from a dynamic perspective, TCs cause the strengthening of cyclonic eddies, leading to positive potential vorticity anomalies, then accelerates the currents and exacerbates global warming, ultimately further promotes TCs enhancement (Zhang et al, 2020)....

删除了: general

删除了: typhoon

89 affected by the TC, and eddies with shorter lifespans or smaller radii are more susceptible to the influence  
90 of TCs. The dynamic adjustment process of eddy and the upwelling induced by TC itself leads to changes  
91 in the three-dimensional structure of the cyclonic eddies, including ellipse deformation and re-  
92 axisymmetrization on the horizontal plane, resulting in eddy intensification. The presence of cold eddies  
93 not only exacerbates the sea surface cooling in the post-TC cold eddy region but also accompanies a  
94 decrease in sea level anomaly (SLA), deepening of the mixed layer, a strong cooling in the subsurface,  
95 increased chlorophyll-a concentration within the eddy, and substantial increases in EKE and available  
96 potential energy (Shang et al., 2015; Liu and Tang, 2018; Li et al., 2021; Ma et al., 2021).

97 Generally, TCs lead to a weakening of warm eddies, while the sea surface cooling is not significant,  
98 typically within 1°C. However, there is a noticeable cooling and increased salinity in the subsurface layer,  
99 accompanied by an upward shift of the 20°C isotherm, a decrease in heat and kinetic energy (Lin et al.,  
100 2005; Liu et al., 2017; Huang and Wang, 2022). Lu et al. (2020) propose that TCs primarily generate  
101 potential vorticity input through the geostrophic response. When a TC passes over an eddy, there is a  
102 significant positive wind stress curl within the TC's maximum wind radius ( $R_{max}$ ), which induces  
103 upwelling in the mixed layer due to the divergence of the wind-driven flow field. This upward flow  
104 compresses the thickness of the isopycnal layers below the mixed layer, resulting in a positive potential  
105 vorticity anomaly. Rudzin and Chen (2022) find that under the interaction of the strong TC wind stress  
106 in the eye area of the TC and the subsurface ocean current, the positive vertical vorticity advection caused  
107 the TC to eliminate the warm eddy from bottom to top after passing through. However, the projection of  
108 TC wind stress onto the eddy and the relative position of the warm eddy to the TC can lead to different  
109 responses. According to the classical description of TC-induced upwelling, strong upwelling occurs  
110 within two-times  $R_{max}$  of the TC center, while weak subsidence exists in the vast area outside the  
111 upwelling region (Price, 1981; Jullien et al., 2012). The warm eddy, located directly beneath the TC's  
112 path weakens due to the cold suction caused by the TC's center. However, for warm eddies located  
113 beyond two-times  $R_{max}$ , they are influenced by the TC's wind stress curl and the downwelling within  
114 the eddy itself, resulting in the convergence of warm water in the upper layers of the eddy, an increase  
115 in mixed layer thickness, and an increase in heat content, leading to a warming response to the TC (Jaimés  
116 and Shay, 2015).

117 The NSCS encounters high frequency and intense TCs, concurrently, there is notable activity of  
118 mesoscale eddies in this region. Based on in-situ datasets, multi-platform satellite measurements, and

删除了: typhoon

删除了: typhoon

删除了: typhoons

删除了: reduction

删除了: typhoons

删除了: typhoon

删除了: typhoon's

删除了: By analyzing the time series of ocean kinetic energy, available potential energy (APE), vorticity budget, and potential vorticity (PV) budget,

删除了: Under the interaction of the strong TC wind stress in the eye area of the typhoon and the subsurface ocean current field, the early-onset of a near-inertial wake caused the disappearance of the warm eddy....

删除了: typhoon

删除了: twice

删除了: the

删除了: maximum wind radius

删除了: typhoon

删除了:

删除了: locates

删除了: typhoon's

删除了: typhoon's

删除了: locate

删除了: twice the maximum wind radius

删除了: typhoon's

删除了: typhoon

删除了: tropical cyclones (

删除了: )

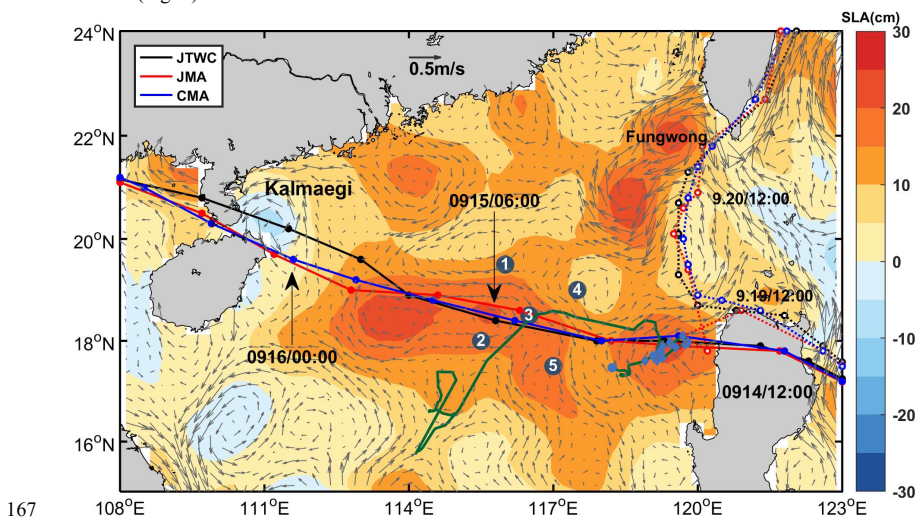
148 GLORYS12V1 reanalysis data, we investigate [how the upper ocean in](#) two anticyclonic eddies [responds](#)  
149 to Typhoon Kalmaegi. This marks the initial effort to characterize the different physical variations  
150 induced by TCs within two same polarity eddies, contributing to a better understanding [of](#) the role played  
151 by mesoscale eddies in modulating interactions between TCs and the ocean. Section 2 provides an  
152 overview of the data and methods utilized in this research. Section 3 analyzes the physical parameters of  
153 warm eddies, vertical temperature and salinity variations, and explores the different responses of warm  
154 eddies both inside and outside the typhoon affected region. Section 4 offers a comprehensive discussion  
155 and Section 5 gives a summary.

删除了: on upper ocean responses

## 156 2. Data and Methods

### 157 2.1. Data

158 The six-hourly best-track typhoon datasets are obtained from the Joint Typhoon Warning Center  
159 (JTWC, <http://www.usno.navy.mil/JTWC>, last access: 3 February, 2021), the Japan Meteorological  
160 Agency (JMA, <https://www.jma.go.jp/jma/jma-eng/jma-center/rsmc-hp-pub-eg/besttrack.html>, last  
161 access: 3 February, 2021), and the China Meteorological Administration (CMA,  
162 <http://tcdata.typhoon.gov.cn>, last access: 3 February, 2022). The data contain the TCs' center locations,  
163 the minimum central pressure, maximum sustained wind speed, and intensity category. The translation  
164 speed of typhoons is calculated by dividing the distance travelled by each typhoon within a 6-hour  
165 interval by the corresponding time. In this paper, Typhoon Kalmaegi and tropical storm Fung-wong are  
166 studied (Fig. 1).



167

169 **Figure 1.** The tracks of Typhoon Kalmaegi (solid lines with dots) and tropical storm Fung-wong (dashed lines with  
 170 hollow dots) as provide by the Joint Typhoon Warning Center (JTWC, black), Japan Meteorological Agency (JMA,  
 171 red), and China Meteorological Administration (CMA, blue). The colour shading represents the sea surface level  
 172 anomaly on 13 September, 2014, while the gray arrows illustrate the geostrophic flow field. The numbered blue dots  
 173 represent the positions of the five buoy/mooring stations, the green line illustrates the trajectory of Argo 2901469,  
 174 and the blue diamond's mark the positions of Argo 2901469 inside the eddy AE2 from 26 August 2014 to 25 October  
 175 25, 2014.

176 The daily Sea Level Anomaly (SLA) and geostrophic current data [are provided](#) by Archiving,  
 177 Validation, and Interpretation of Satellite Data in Oceanography (AVISO) product (CMEMS,  
 178 <https://marine.copernicus.eu/>, last access: 14 [February](#), 2022). This dataset combines satellite data from  
 179 Jason-3, Sentinel-3A, HY-2A, Saral/AltiKa, Cryosat-2, Jason-2, Jason-1, T/P, ENVISAT, GFO, and  
 180 ERS1/2. The spatial resolution of the product is  $1/4^\circ \times 1/4^\circ$ . [The period from 1 September to 30](#)  
 181 [September 2014](#) was used.

182 The daily Sea Surface Temperature (SST) data used in this study is derived from the Advanced Very  
 183 High-Resolution Radiometer (AVHRR) product data provided by the National Oceanic and Atmospheric  
 184 Administration (NOAA). The data is obtained from the Physical Oceanography Distributed Active  
 185 Archive Center (PODAAC) at the NASA Jet Propulsion Laboratory (JPL)  
 186 ([ftp://podaac.jpl.nasa.gov/documents/dataset\\_docs/avhrr\\_pathfinder\\_sst.html](ftp://podaac.jpl.nasa.gov/documents/dataset_docs/avhrr_pathfinder_sst.html), last access: 16 March,  
 187 2022). The spatial resolution of the data is  $1/4^\circ \times 1/4^\circ$ .

188 Argo data, including profiles of temperature and salinity from surface to 2000 m depth are obtained  
 189 from the real-time quality-controlled Argo data base (Euro-Argo, <https://dataselection.euro-argo.eu/>, last  
 190 access: 4 April, 2022). We select Argo float number 2901469, situated in an [anticyclonic eddy](#) and in  
 191 close proximity to [Typhoon Kalmaegi](#), both before and after the typhoon's passage in 2014. Profiles of  
 192 this Argo are also used to validate the vertical distribution of temperature and salinity from  
 193 GLORYS12V1.

194 For this study, we also utilize in-situ data from a cross-shaped array consisting of five stations,  
 195 comprising five moored buoys and four subsurface moorings (refer to Fig. 1). More specific information  
 196 can be found in Zhang et al. (2016). To investigate the impact of the typhoon on a warm eddy, we select  
 197 the temperature and salinity data from Station 5, [situated to the left of Kalmaegi's track](#).

198 The wind speed data is sourced from the European Centre for Medium-Range Weather Forecasts  
 199 (ECMWF) ERA-Interim reanalysis assimilation dataset ([https://apps.ecmwf.int/datasets/data/interim-  
 200 full-daily/levtype=sfc/](https://apps.ecmwf.int/datasets/data/interim-full-daily/levtype=sfc/), last access: 5 January, 2023). [We used](#) the reanalysis data of surface winds at a  
 201 height of 10 meters above sea level for TCs. The selected data has a spatial resolution of  $1/4^\circ \times 1/4^\circ$  and  
 202 a temporal resolution of 6 hours, with four updates per day (00:00, 06:00, 12:00, and 18:00 UTC). The  
 203 data [corresponds to September 2014](#).

204 The Global Ocean Reanalysis Product GLOBAL [MULTIYEAR\\_PHY\\_001\\_030](#) (GLORYS12V1),  
 205 provides by the Copernicus Marine Environment Monitoring Service (CMEMS,  
 206 <https://marine.copernicus.eu/>, last access: 23 March, 2022) is used in this study too. This reanalysis  
 207 product utilized the NEMO 3.1 numerical model coupled with the LIM2 sea ice model, and forced with

删除了: Febururay

删除了: ,

删除了: t

删除了: ocean

删除了: typhoon

删除了: situates

删除了: along

删除了: track of

删除了: This dataset is widely used for weather analysis and numerical forecasting. The wind field data used in this study primarily focuses

删除了: on

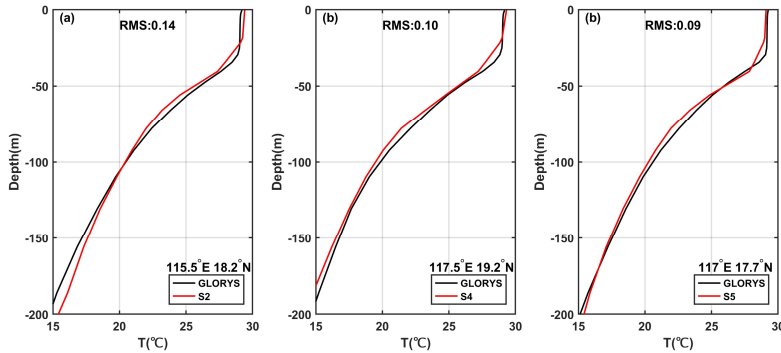
删除了: utilize

删除了: REA- NALYSIS

设置了格式: 非突出显示

222 ERA-Interim atmospheric data. The model assimilated along-track altimeter data from satellite  
 223 observations (Pujol et al., 2016), satellite sea surface temperature data from AVHRR, sea ice  
 224 concentration from CERSAT (Ezraty et al., 2007), and vertical profiles of temperature and salinity from  
 225 the CORAv4.1 database (Cabanes et al., 2012). The temperature and salinity biases were corrected using  
 226 a 3D-VAR scheme. The horizontal resolution is  $1/12^\circ \times 1/12^\circ$ , and it has 50 vertical levels. The  
 227 temperature, salinity and ocean mixed layers thickness from 1 September to 30 September 2014 were  
 228 chosen.

229 GLORYS12V1 is a widely used and applicable dataset, to evaluate its temperature profiles, in-situ  
 230 data of Station 2, Station 4 and Station 5 were compared (Fig. 2). Since the GLORYS12V1 data  
 231 assimilates with the data of Argo floats, it demonstrates good agreement with Argo profiling floats, the  
 232 maximum difference between them is less than  $0.2^\circ\text{C}$ , the Root Mean Square (RMS) is 0.02 (Figure not  
 233 shown). However, there are some discrepancies between the GLORYS12V1 and the Station 5 data, with  
 234 the largest difference occurring at the depths of 30 m (mixed layer) and 78 m (thermocline), both differing  
 235 by  $0.6^\circ\text{C}$ , while below 150 m, the difference is quite small. The RMS is 0.09. The RMS between  
 236 GLORYS12V1 and Station 2 (Station 4) is 0.14 (0.10), with deviations in the mixed layer and  
 237 thermocline. Although compared to S5, the RMS of S2 and S4 is a little larger, but still acceptable.  
 238 Overall, GLORYS12V1 reproduces the observed ocean temperature accurately, it is reasonable to use it  
 239 to investigate the vertical response of anticyclonic eddies to Typhoon Kalmaegi.



240 **Figure 2.** Evaluation of GLORYS12V1 data performance during September 2014. (a), (b) and (c) are the comparison  
 241 of vertical monthly mean temperatures recorded at stations 2(115.5°E 18.2°N), Station 4 (117.5°E 19.2°N) and  
 242 Station 5 (117°E 17.7°N) respectively.

## 244 2.2. Methods

245 Vorticity is a vector that characterizes the local rotation within a fluid flow. Mathematically, it is  
 246 defined as the curl of the velocity vector. In most cases, when referring to vorticity, it specifically pertains  
 247 to the vertical component of the vorticity. It is calculated from:

$$248 \zeta = \frac{\partial v}{\partial x} - \frac{\partial u}{\partial y} \quad (1)$$

- 删除了: and
- 删除了:
- 删除了: form
- 删除了: to study
- 删除了: the Argo profiles and
- 删除了: The
- 删除了: exhibit
- 删除了: (Figures not shown).
- 删除了: Because the GLORYS12V1 assimilates with Argo data and the vertical resolution of upper 100 m in Argo profile is 5 m, but the vertical interval of buoy array is 20 m.[RE-WRITE] Therefore, the large deviations exist at mixed layer and thermocline during the typhoon in in-situ data of Station 5.
- 删除了: by
- 删除了: typhoon
- 设置了格式: 字体: 非加粗
- 设置了格式: 字体: 非加粗
- 设置了格式: 字体: 非加粗
- 设置了格式: 字体: 非加粗
- 删除了: (a) Vertical monthly mean temperature within the anticyclonic eddy AE2 (119.5°E 17.9°N) as measured by Argo float 2901469. (b) Comparison of vertical monthly mean temperature recorded at Station 5 (117°E 17.7°N).
- 设置了格式: 字体: 加粗, 英语(美国)

268  $u$  and  $v$  are the zonal (eastward) and meridional (northward) geostrophic velocities, respectively. They  
 269 are derived from altimeter sea level anomaly data ( $\eta$ ):

$$270 \quad u = -\frac{g}{f} \frac{\partial \eta}{\partial y}, v = \frac{g}{f} \frac{\partial \eta}{\partial x}. \quad (2)$$

271 Here,  $g$  is the acceleration of gravity,  $f$  is the Coriolis frequency. Vorticity is considered a  
 272 fundamental characteristic of mesoscale eddies, positive vorticity signifies cyclonic eddies, while  
 273 negative vorticity indicates anticyclonic eddies.

274 The Rossby number (Ro) is a dimensionless number describing fluid motion, and it is the ratio of  
 275 relative vorticity to planetary vorticity, reflecting the relative importance of local non-geostrophic motion  
 276 [versus](#) large-scale geostrophic motion. The larger the Rossby number, the stronger the local non-  
 277 geostrophic effect, and the definition of this parameter is:

$$278 \quad Ro = \frac{\zeta}{f}. \quad (3)$$

279 Eddy Kinetic Energy (EKE) is a measure of the energy associated with mesoscale eddies, which  
 280 indicates the intensity of eddies. It is typically calculated using the anomalies of the geostrophic velocity:

$$281 \quad EKE = \frac{1}{2}(u'^2 + v'^2), \quad (4)$$

282 where  $u'$  represents the anomaly of the geostrophic zonal (eastward) velocity,  $v'$  represents the anomaly  
 283 of the meridional (northward) velocity. [The geostrophic velocity anomalies are referenced to the period](#)  
 284 [of 1993 to 2012.](#)

285 To evaluate the impact of a typhoon on an anticyclonic eddy, the calculation begins with determining  
 286 the wind stress:

$$287 \quad \vec{\tau} = \rho_a C_d U_{10} \overline{U_{10}}, \quad (5)$$

288 where  $\rho_a$  is the air density, assumed to be a constant value of  $1.293 \text{ kg m}^{-3}$ ,  $U_{10}$  represents the 10-  
 289 meter wind speed. And  $C_d$  is the drag coefficient at the sea surface (Oey et al., 2006):

$$290 \quad C_d \times 1000 = \begin{cases} 1.2 & U_{10} \leq 10 \text{ m s}^{-1} \\ 0.49 + 0.65U_{10} & 11 \leq U_{10} < 19 \text{ m s}^{-1} \\ 1.364 + 0.234U_{10} - 0.00023158U_{10}^2 & 19 \leq U_{10} \leq 100 \text{ m s}^{-1} \end{cases}. \quad (6)$$

291 The wind stress curl is calculated by (Kessler, 2006):

$$292 \quad curl(\vec{\tau}) = \frac{\partial \tau_y}{\partial x} - \frac{\partial \tau_x}{\partial y}, \quad (7)$$

293 where  $\tau_x$  and  $\tau_y$  are the eastward and northward wind stress vector components, respectively. The curl  
 294 represents the rotation experienced by a vertical air column in response to spatial variations in the wind  
 295 field.

296 The Ekman pumping velocity (EPV) represents the ocean upwelling rate, which can be used to study  
 297 the contribution of typhoons to regional ocean upwelling. Positive means upwelling, negative represents  
 298 downwelling:

$$299 \quad EPV = curl\left(\frac{\vec{\tau}}{\rho_f}\right), \quad (8)$$

删除了: to

301 where the wind stress is obtained from Eq. (7),  $\rho$  is seawater density, the value is  $1025 \text{ kg m}^{-3}$ , and  $f$   
302 is the Coriolis frequency.

303 The buoyancy frequency is a measure of the degree to which water is mixed and stratified. In a stable  
304 temperature stratification, the fluid particles move in the vertical direction after being disturbed, and the  
305 combined action of gravity and buoyancy always makes them return to the equilibrium position and  
306 oscillate due to inertia. When  $N^2 < 0$ , the water is in an unstable state:

$$307 \quad N^2 = -\frac{g}{\rho} \frac{\partial \rho}{\partial z} \quad (9)$$

308 where  $\rho$  is seawater density,  $g$  is the acceleration of gravity, and  $z$  is the depth.

### 309 3. Results

#### 310 3.1. Typhoon and pre-existing eddies in the NSCS

##### 311 3.1.1. Track of Typhoon Kalmaegi and tropical storm Fung-wong

312 Typhoon Kalmaegi strengthens into a typhoon by 1200 UTC on 13 September and emerged over the  
313 warm waters of the Northern South China Sea (NSCS) by 1500 UTC on 14 September, with maximum  
314 sustained winds of  $33 \text{ m s}^{-1}$  (Fig. 3-4). During this period, the NSCS experiences predominantly weak  
315 vertical wind shear and is characterized by multiple anticyclonic warm eddies (Fig. 3). Subsequently,  
316 Typhoon Kalmaegi undergoes two rapid intensification phases between 15 and 16 September. The first  
317 intensification occurs at 0000 UTC on 15 September, propelling Kalmaegi to category 1 status with  
318 surface winds surpassing  $35 \text{ m s}^{-1}$ . By 1200 UTC on 15 September, Kalmaegi experiences a second, even  
319 more rapid intensification, with winds reaching  $40 \text{ m s}^{-1}$  in less than 12 hours. Throughout this  
320 intensification stage, Kalmaegi encounters two warm eddies: anticyclonic eddy AE1, is positioned to the  
321 left of the typhoon's path, with its core situated on the periphery of the typhoon's one-times  $R_{max}$   
322 (Fig.3c-d), AE1 has a lifespan of 105 days from 26 June to 8 October and is positioned at  $17^\circ\text{N}$ - $20^\circ\text{N}$ ,  
323  $113^\circ\text{E}$ - $116^\circ\text{E}$ . AE2 precisely intersects with the typhoon's trajectory, and its core nearly coincides with  
324 the  $R_{max}$  of the typhoon (Fig.3b-d). It has a lifespan of 89 days from 24 August to 20 November and is  
325 located at  $17^\circ\text{N}$  - $19^\circ\text{N}$ ,  $118^\circ\text{E}$  - $120^\circ\text{E}$ . Kalmaegi makes landfall on Hainan Island at 0300 UTC on 16  
326 September, with a minimum central pressure of 960 hPa and a maximum wind speed of  $40 \text{ m s}^{-1}$ . After  
327 landfall, Typhoon Kalmaegi gradually weakens and dissipates. During its crossing of the NSCS, the five  
328 mooring stations are affected. Stations 1 and 4 are on the right side of Typhoon Kalmaegi's track, while  
329 Stations 2 and 5 are on the left side. Unfortunately, the wire rope of the buoy at Station 3 is destroyed by  
330 Kalmaegi, resulting in missing data from 15 September. Among the stations, Station 5 is on the left of  
331 typhoon track and outside AE2, so its data is used in our study.

332 Tropical storm Fung-wong initially moves quickly in a northwest direction after formation. On 19  
333 September, it enters the Luzon Strait and decelerates. It makes landfall in Taiwan on the 21 September

删除了: m

删除了: m

删除了: situates

删除了: Throughout this intensification stage, Kalmaegi encounters two warm eddies: anticyclonic eddy AE1, locates to the left of the typhoon's path, its core situates on the periphery of two times maximum wind radius of typhoon (Fig.3c-d)

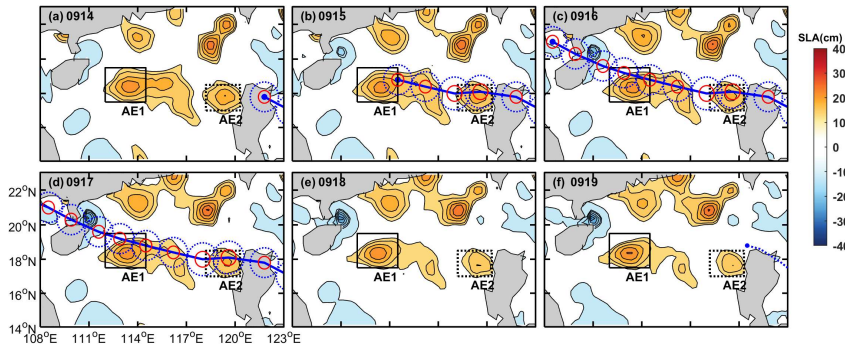
删除了: ing

删除了: AE2, precisely intersecting with the typhoon's trajectory, its core almost coincident with maximum wind radius of typhoon (Fig.3b-d)....

删除了: .



346 and subsequently lands in Zhejiang on the 22 September before gradually dissipating. When crossing the  
 347 Luzon Strait at 1200 UTC on 19 September, anticyclonic eddy AE2 is on the left side of Fung-wong,  
 348 with a distance of just over 100 km from its center.



349 **Figure 3.** The variations in sea level anomaly before and after Typhoon Kalmaegi moved over the anticyclonic eddies  
 350 AE1 and AE2 between 14 September and 19 September (a-f). The black solid rectangle represents the area of AE1,  
 351 while the black dashed rectangle represents the area of AE2. The blue solid line depicts the path of Typhoon  
 352 Kalmaegi, the solid red and dashed blue circles are the one-times  $R_{max}$  of the typhoon and width of typhoon-  
 353 induced baroclinic geostrophic response, while the blue dotted line in (f) is the path of tropical storm Fung-wong  
 354 (best-track data sourced from CMA).  
 355

### 356 3.1.2. Eddy characteristics distribution

357 Satellite SLA measurements have proven to be highly effective and widely used for identifying and  
 358 quantifying the intensity of ocean eddies (Li et al., 2014). In Fig. 3, two warm eddies with clear positive  
 359 ( $>13$  cm) SLA are observed along the Typhoon Kalmaegi's track. During the period of 15 to 16  
 360 September, the typhoon passes over two warm anticyclonic eddies, AE1 and AE2. Before the typhoon,  
 361 AE1 is the most prominent eddy in the SCS, with an amplitude of 23.0 cm, and a radius of 115.5 km.  
 362 AE2, located west of Luzon Island, has an amplitude of 21.2 cm, with a radius of approximately 65.5  
 363 km. Tracing back to 2 months (figure is not shown), AE1 propagates slowly westward with about  $0.1$  m  
 364  $s^{-1}$ , while AE2 is generated on 24 August. During 14 to 19 September, the amplitude of AE1 increases  
 365 1.3 cm. The area of the AE1 decreases by approximately 31% from  $1.3 \times 10^5$  km<sup>2</sup> to  $9.1 \times 10^4$  km<sup>2</sup> and  
 366 splits into two eddies. When Typhoon Kalmaegi crosses the core of AE2 at 1500 UTC on 14 September,  
 367 and tropical storm Fung-wong moves over the northeast of AE2 at 1200 UTC on 19 September, the  
 368 amplitude decreases by 3.1 cm. The area of the AE2 decreases by approximately 36% from  $4.2 \times 10^4$  km<sup>2</sup>  
 369 to  $2.7 \times 10^4$  km<sup>2</sup>.

370 Because of intense solar radiation in September, the SST in the SCS is generally above  $28.5^\circ\text{C}$  prior  
 371 to the arrival of Typhoon Kalmaegi (Fig. 4a). As a fast-moving typhoon with a mean moving speed of  
 372 over  $8$  m  $s^{-1}$ , Kalmaegi induces a larger cooling area and intensity on the right side of its path compared  
 373 to the left side (Price, 1981). During the passage of Kalmaegi, the lowest SST on the right side of typhoon  
 374 decreases to  $27.2^\circ\text{C}$ . Even after the typhoon has passed, a cold wake could still be observed on the right  
 375 side of its path, persisting for over a week (Fig. 4c).

删除了: typhoon  
 删除了: - and two  
 删除了: maximum wind radius

删除了: typhoon

删除了: locates  
 删除了: exhibits  
 删除了: m

删除了: .

384 The pre-existing warm eddy AE1 begins to cool down before Kalmaegi reached the NSCS, dropping  
 385 to 28.4°C on 14 September. During this period, the mean SST within AE1 increases slightly to 28.6 °C  
 386 (Fig. 5a). However, as cooler water from the right side of the typhoon track is subsequently advected into  
 387 the AE1 region (Fig. 4c), the SST decreases and reaches 28.0 °C on September 19, which is 0.4°C lower  
 388 than that before the typhoon. The average SST drop in AE1 is evident, with SST starting to decline before  
 389 14 September and reaching its lowest temperature (28.1°C) on 15 September, 0.6 °C lower than that  
 390 before the typhoon (Fig. 5c). On 16 September, the SST within AE2 begins to recover, but it starts to  
 391 cool again on 18 September due to the influence of Fung-wong.

392 Then we compare the Ro and EKE of AE1 and AE2 before, during and after typhoon. Before being  
 393 influenced by the typhoon, the warm eddy AE1 exhibits a more scattered distribution of negative Ro due  
 394 to its edge structure, and the EKE values at the eddy boundary are relatively high (Fig. 4d, g). As the  
 395 typhoon passes through the eddy, the Ro and EKE of AE1 increase. On 19 September, the average Ro  
 396 within AE1 reaches a value of  $-8.2 \times 10^{-2}$ , at the same time, the average EKE increases to its maximum  
 397 value of  $325.0 \text{ cm}^2 \text{ s}^{-2}$ . The variation trend of Ro and EKE within the eddy is consistent, increasing from  
 398 the passage of the typhoon and starting to recover on 20 September (Fig. 5b-c). This indicates that  
 399 although the area of the warm eddy AE1 decreased under the influence of the typhoon, its intensity  
 400 increases. On the other hand, for warm eddy AE2, both Ro and EKE decreases after the typhoon passage,  
 401 with the Ro decreasing to  $-4.5 \times 10^{-2}$  on 17 September and the EKE decreasing to  $152.0 \text{ cm}^2 \text{ s}^{-2}$  on the 19  
 402 September, following by a recovery (Fig. 5f-g). Unlike AE1, AE2 weakens in intensity under the  
 403 influence of the typhoon.

404 During the passage of the typhoon, wind stress-driven mixing enhancement and an increase in vertical  
 405 shear result a deepening of the MLD, which further strengthens the mixing between the deep cold water  
 406 and the upper warm water (Shay and Jaimes, 2009). To avoid a large part of the strong diurnal cycle in  
 407 the top few meters of the ocean, 10 m is set as the reference depth (De Boyer Montégut, 2004). A 0.5 °C  
 408 threshold difference from 10 m depth is calculated and defined as the MLD (Thompson and Tkalich,  
 409 2014). Prior to the influence of typhoon Kalmaegi, the MLD in the AE1 and AE2 regions is deeper (Fig.  
 410 4j), with the average MLDs of 32 m and 33 m, respectively. Starting from 14 September, the MLDs are  
 411 influenced by typhoon Kalmaegi, with the MLD of AE1 deepening to 37 m and that of AE2 increasing  
 412 to 41 m, representing a deepening of 5 m and 8 m, respectively (Fig. 5d, h).

413 Overall, Typhoon Kalmaegi likely exerts distinct impacts on the two warm eddies. Despite both AE1  
 414 and AE2 experiencing a decrease in their respective areas by approximately one-third, accompanied by  
 415 deepening of the MLD, the amplitude of SLA within AE1 increases by 1.3 cm, whereas AE2 witnesses  
 416 a decrease of about 3.1 cm in its amplitude. Furthermore, the SST, Rossby number and EKE within AE1  
 417 and AE2 exhibited contrasting patterns.

删除了: Mesoscale eddies, due to their special thermodynamic structure and varying positions in relation to the TC, can modulate distinct sea surface temperature changes and exhibit different characteristics. ...

删除了: relatively

删除了: starts to

删除了:  $\text{cm}^2$

删除了: follows

删除了: weakens

删除了: enhances

删除了: driven by wind stress

删除了: s

设置了格式: 非突出显示

设置了格式: 非突出显示

设置了格式: 非突出显示

设置了格式: 非突出显示

设置了格式: 突出显示

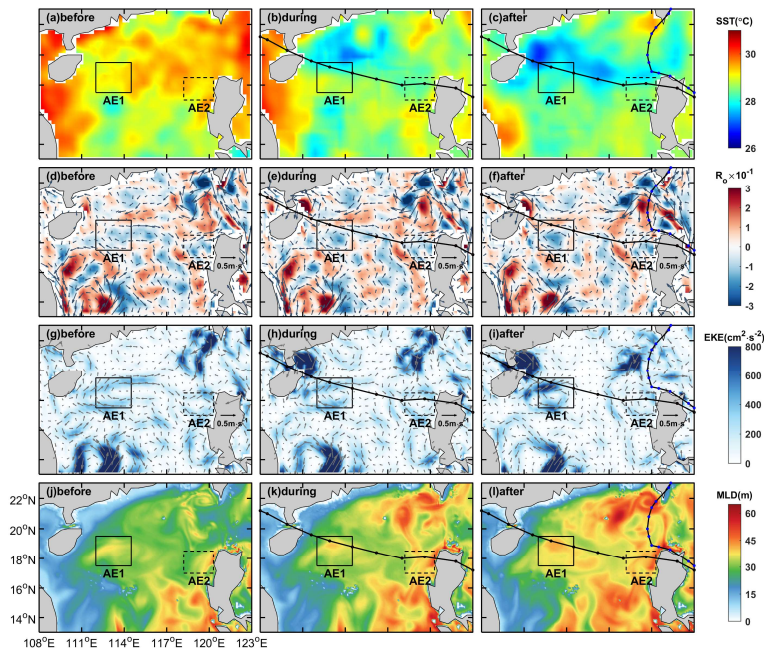
删除了: [RE-WRITE]

删除了: in

删除了: defines

删除了: accompanies

删除了: exhibits



435

436

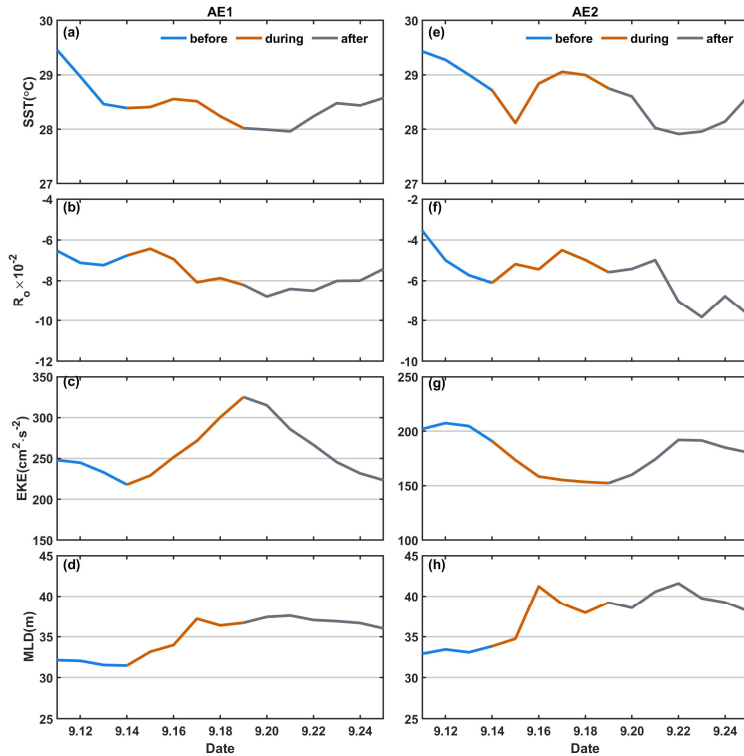
437

438

439

440

**Figure 4.** The spatial distribution of SST,  $R_o$ , EKE, and MLD before, during and after the passage of TCs. The time periods of 10-13, 15-16 and 19-22 September are designated as stages before, during and after Kalmaegi, respectively. The path of Typhoon Kalmaegi is depicted by a black solid line with black dots, while the path of tropical storm Fung-wong is represented by a black solid line with blue dots in the third column. The solid and dashed boxes correspond to AE1 and AE2, respectively.



441 **Figure 5.** The time series of sea surface temperature (SST),  $R_\sigma$ , eddy kinetic energy, and mixed layer depth (MLD)  
 442 within the warm eddies' regions (black solid and dashed boxes in Fig. 4). The first column is variables of AE1, the  
 443 second column is for AE2.  
 444

445 **3.2 Upper-ocean vertical thermal and salinity structure of eddies**

446 We conducted further analysis on the vertical temperature and salinity structure of the warm eddies  
 447 AE1 and AE2 before and after the Typhoon Kalmaegi using GLORYS12V1 data. During the typhoon's  
 448 passage on 15 September, the temperature above the MLD within AE1 increases by approximately 0.1 °C,  
 449 while the salinity decreases by 0.02psu (Fig. 6). Below the MLD, the temperature shows a significant  
 450 increase, reaching a maximum temperature rise of 1.3 °C. Correspondingly, the salinity below the MLD  
 451 exhibits a decrease of 0.05 psu. Vertical temperature on Kalmaegi's arrival day shows warm pattern from  
 452 surface to 200 m, the salinity shows "fresher-saltier" pattern. These changes lead to a deepening of  
 453 isopycnals by 15 m and a decrease in buoyancy frequency  $N^2$  (Fig. 7a-b), indicating convergence and  
 454 downwelling within the centre of the warm eddy AE1. The near-inertial waves propagates downward  
 455 from surface to 200m during this period (Zhang et al, 2016). The transfer of energy from anticyclonic  
 456 eddy to near-inertial waves is the main reason for the downward propagation and longtime persistence  
 457 of near-inertial energy (Chen et al., 2023).

删除了: conductes

删除了: the isodensity

删除了: [?]

删除了: from

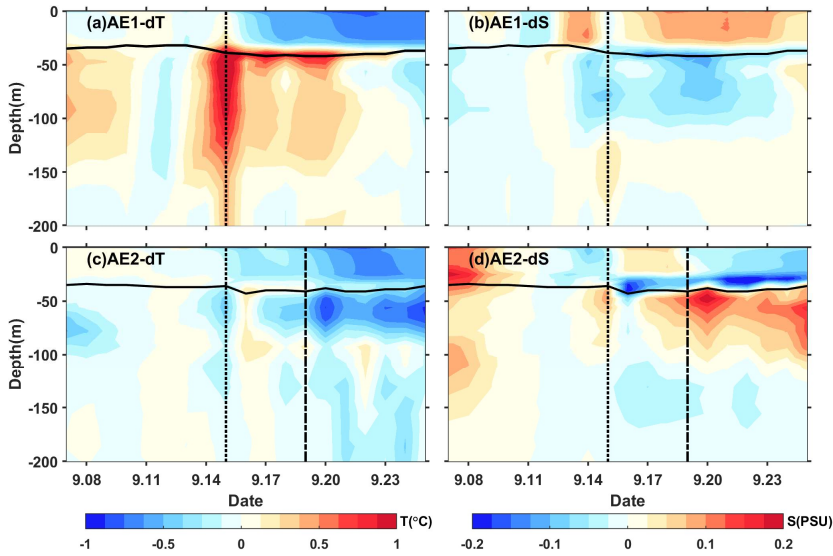
删除了: proppagation

463 After 15 September, the temperature above the MLD decreases, and the salinity shows an increase  
 464 (Fig. 6a-b), resulting in the uplift of the 1021  $\text{kg m}^{-3}$  isopycnal to the sea surface (Fig. 7a-b). The  
 465 subsurface warming and salinity reduction gradually weakens after the Typhoon Kalmaegi but persists  
 466 for about a week after the typhoon's passage until 22 September. During this period, vertical temperature  
 467 pattern becomes "cool-warm" at the center of AE1, and the salinity distribution pattern becomes "saltier-  
 468 fresher-saltier". This persistence can be attributed to the intensified stratification around the MLD, with  
 469  $N^2$  around  $9.0 \times 10^{-4} \text{s}^{-2}$  (Fig. 7b). The increased stability inhibits vertical mixing, restrains the exchange  
 470 of heat and salinity, and leads to smoother density gradients above the MLD (Fig. 7a).

471 The vertical temperature and salinity structure of AE2 exhibits an opposite trend. During the typhoon  
 472 passage on 15 September, AE2 also experiences a cooling trend of  $0.2 \text{ }^\circ\text{C}$ , with a decrease in salinity of  
 473  $0.04 \text{ psu}$  above the MLD. Below the MLD, the temperature shows a consistent decrease, with a change  
 474 of less than  $0.5 \text{ }^\circ\text{C}$  within the subsurface. Correspondingly, the salinity exhibits an increase of  
 475 approximately  $0.08 \text{ psu}$  (Fig. 6c-d). The slightly upward shift of the isopycnals (Fig. 7c) suggests the  
 476 possibility of cold-water upwelling induced by the suction effect of the typhoon. The temperature  
 477 decreases and salinity increases below the MLD are primarily driven by upwelling.

478 Furthermore, when the tropical storm Fung-wong passes through AE2 on 19 September (dashed line  
 479 in Fig. 6c-d), the decreasing trend of subsurface temperature becomes more pronounced, and the  
 480 subsurface salinity exhibits a significant increase. AE2 is more significantly influenced by tropical storm  
 481 Fung-wong. It presents stable stratification with  $N^2$  around  $8.4 \times 10^{-4} \text{s}^{-2}$  at a depth of 42 m, creating a  
 482 barrier layer that prevents the intrusion of high-salinity cold water from the lower layers into the mixed  
 483 layer (Yan et al., 2017).

484

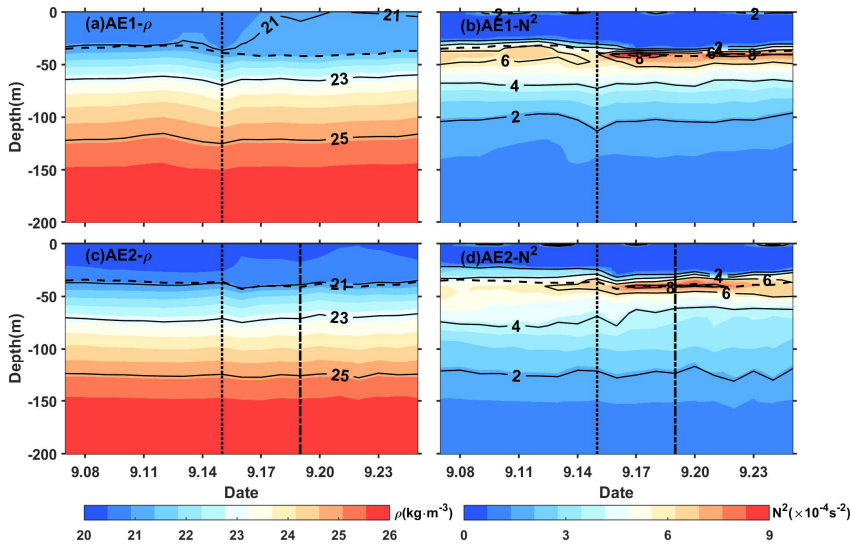


485

删除了: kg  
 删除了: isodensity

删除了: isodensity  
 删除了:  
 删除了: processes

491 **Figure 6.** The timeseries of vertical temperature and salinity anomalies in the center of AE1(a,b) and AE2 (c,d).  
 492 The anomalies were calculated relative to the average value of 10-13 September. The vertical black dotted line  
 493 indicates the Typhoon Kalmaegi's passage, while the vertical black dashed line represents the passage of tropical  
 494 storm Fung-wong. The black solid line is the MLD.



495  
 496 **Figure 7.** Same as Fig. 7, but for density and buoyancy frequency ( $N^2$ ).

### 497 3.3 Comparison of the response between eddies and non-eddies areas

498 To investigate the contrasting response of warm eddies and the non-eddies background to Typhoon  
 499 Kalmaegi, we conduct a comparative analysis of vertical temperature and salinity profiles in these two  
 500 areas. Unfortunately, there is no Argo data around AE1, therefore, we examine data from Argo 2901469,  
 501 which is located within AE2 during the period from 11 to 19 September. The temperature and salinity  
 502 data from Station S5 is considered as the background, with S5 located at a distance of 246 km from  
 503 AE2's center on 15 September (Fig. 1). These profiles are categorized into three periods: pre-typhoon  
 504 (11 September), during-typhoon (15 September), and post-typhoon (19 September).

505 At depths above 40m, both the inside and outside of AE2 experience a decrease in temperature, with  
 506 a cooling of less than  $-1.0^{\circ}\text{C}$ . Four days after the typhoon passage (19 September), the cooling persists  
 507 inside and outside the eddy, with the cooling being more pronounced outside AE2, showing a decrease  
 508 of  $1.2^{\circ}\text{C}$  (Fig. 8c). The salinity within AE2 initially increases by 0.15 psu from the pre-typhoon stage to  
 509 the during-typhoon stage and then decreases by 0.09 psu after the typhoon passage (Fig. 8d). While the  
 510 salinity at Station 5 shows a similar pattern in pre-typhoon and during-typhoon stage, it increases by 0.05  
 511 psu after the typhoon. Two possible processes can explain the difference in salinity trends inside and  
 512 outside AE2. First, during the pre-typhoon to typhoon stage, the entrainment within AE2 may have  
 513 brought the subsurface water, which is saltier, up to the surface, resulting in an increase in salinity. The

删除了: t

删除了: typhoon

删除了: locates

删除了:

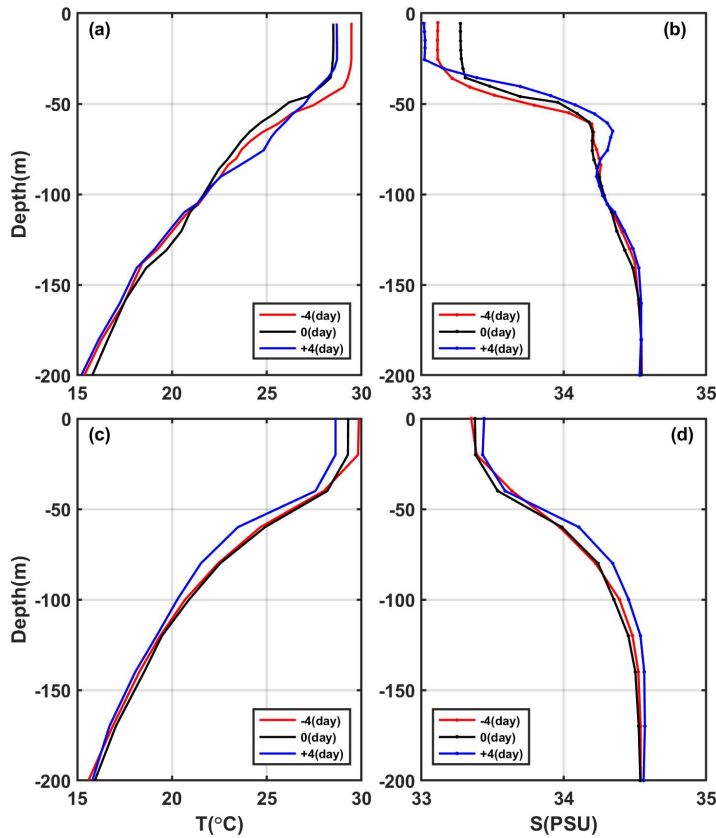
删除了: experiences

删除了:

520 second process is related to the typhoon-induced precipitation after the typhoon passage, which lead to a  
 521 decrease in salinity. Strong stratification has contributed to the persistence of saltier subsurface water.  
 522 While at S5, the increase in salinity is relatively minor.  
 523 On 15 September, the subsurface layer at 45 m to 100 m is affected by the cold upwelling, which is  
 524 caused by the typhoon, resulting in a cooling and increased salinity within AE2. As the forcing of  
 525 Typhoon Kalmaegi diminishes, the upper layer of seawater begins to mix, and warm surface water is  
 526 transported to the subsurface layer. Four days later, a warming phenomenon occurs, with the maximum  
 527 warm anomaly of 1.2 °C observed at a depth of 75 m (Fig. 8a). The mixing effect outside the eddy is not  
 528 significant, resulting in a slight subsurface warming of approximately 0.2 °C, with no significant changes  
 529 in salinity. However, on 19 September, a maximum cold anomaly of -1.2°C is observed at depth of 60  
 530 m, corresponding to the maximum salinity anomaly of 0.13 psu (Fig. 8c-d). Below 100 m, AE2  
 531 experiences a temperature increase of 0.5 °C and a slight decrease in salinity of 0.04 psu. On 19  
 532 September, the temperature and salinity within AE2 show little change. However, outside the eddy, a  
 533 different response is observed. On 19 September, a cooling trend is observed throughout the water  
 534 column, within a range of 0.2 °C, accompanied by a noticeable increase in salinity (Fig. 8c, d), within a  
 535 range of 0.06 psu. This indicates that the typhoon causes a significant upwelling outside the eddy region.

- 删除了: have
- 删除了:
- 删除了: only increased slightly
- 删除了: influences by the downward flow of the eddy itself,
- 删除了: observes
- 删除了:
- 删除了: a
- 删除了: shows
- 删除了:
- 删除了: accompanies
- 删除了:





547  
 548 **Figure 8.** (a-b) the vertical profile of temperature and salt inside the eddy (Argo 2901469), (c-d) the vertical profiles  
 549 of temperature and salt outside the eddy (S5). The red, black and blue lines represent pre-typhoon, during-typhoon  
 550 and post-typhoon stages.

551 Based on Argo profiles and S5 data, the upper ocean above 200 m inside and outside AE2 responds  
 552 differently to the forcing of the typhoon. In the upper layer (0-40 m), cooling is observed both inside and  
 553 outside the eddy, and it lasts longer. In the subsurface layer (45-100m), after the passage of the typhoon  
 554 (19 September), there is a strong cooling outside the eddy, while warming occurs within AE2. Zhang  
 555 (2022) points out that the sea temperature anomalies mainly depend on the combined effects of mixing  
 556 and vertical advection (cold suction). Mixing causes surface cooling and subsurface warming, while  
 557 upwelling (downwelling) leads to cooling (warming) of the entire upper ocean. The temperature anomaly  
 558 in the subsurface layer depends on the relative strength of mixing and vertical advection, with cold  
 559 anomalies dominating when upwelling is strong, and downwelling amplifying the warming anomalies  
 560 caused by mixing. Therefore, due to the strong influence of upwelling outside the eddy, the temperature  
 561 profile of the entire water column shifts upwards, resulting in cooling of the entire upper ocean. On the  
 562 other hand, influenced by the downwelling associated with the warm eddy itself, a warming anomaly of

删除了: for a  
 删除了: duration

删除了: influences  
 删除了:  
 删除了: associates  
 删除了:



569 1.2 °C is observed in the subsurface layer. Compared to region AE2, the cold suction effect caused by  
570 the Typhoon Kalmaegi is still evident in the non-eddy area.

571 In the following sections, we delve into the underlying reasons behind these different responses of  
572 AE1 and AE2 to Typhoon Kalmaegi.

#### 573 4. Discussion

574 TCs influences mesoscale eddies through baroclinic geostrophic response (Lu et al., 2020). The width  
575 of this response is generally constrained within the TC orbit, with the transverse diameter length  
576 represented as (Lu and Shang, 2024)

$$577 L_h = L_d + R_{max} \quad (10)$$

578 Here,  $L_d$  is the first mode of Rossby deformation radius, and  $R_{max}$  denotes the maximum wind  
579 radius.  $L_d = \frac{c}{f}$ , the phase speed of the first baroclinic mode  $c$  was obtained using the method in Jaimes  
580 and Shay (2009). Therefore, the width of Typhoon Kalmaegi-induced baroclinic geostrophic response is  
581 in the range of 92 km (Figure 3). Essentially, these geostrophic effects are caused by wind stress curl,  
582 and the wind stress curl injects disturbance into the ocean through upwelling and downwelling. Most of  
583 the positive wind stress curl exists within  $R_{max}$ , leading to strong upwelling, while the weak negative  
584 wind stress curl occurs outside  $R_{max}$ , resulting in weak subsidence caused by TCs exist outside the  
585 upwelling area (Lu et al., 2020; Lu and Shang, 2024). Typhoon Kalmaegi strengthened after passing  
586 through the warm ocean characteristics of AE2, causing a reduction in  $R_{max}$ . When passing AE1,  $R_{max}$   
587 is 37 km. Notably, the center of AE1 is located outside the  $R_{max}$  (Figure 3). Hence, the hypothesis  
588 presented here suggests that the observed intensification of AE1 on the left side of the typhoon track is  
589 more likely attributed to the negative wind stress curl generated outside the  $R_{max}$ , thereby driving the  
590 enhancement of downwelling in the pre-existing anticyclonic feature in the ocean.

591 The EPV is very small before the typhoon, measuring less than  $0.5 \times 10^{-5} \text{ m} \cdot \text{s}^{-1}$  in both AE1 and AE2.  
592 However, during 15-16 September (Fig. 9c-f), when typhoon crosses the NSCS, the EPV undergoes  
593 significant changes. Its absolute value increases to over  $1.5 \times 10^{-4} \text{ m} \cdot \text{s}^{-1}$  within both AE1 and AE2. AE1  
594 consistently exhibits a predominantly negative EPV during most of this period. Consequently, during  
595 Typhoon Kalmaegi, the negative EPV facilitates downwelling and convergence (Jaimes and Shay, 2015),  
596 leading to a warmer and fresher subsurface layer in AE1 (Fig. 6 a-b). On the other hand, AE2 displays a  
597 more fluctuating pattern. It is positive on 14 September, shows both positive and negative values at 0000  
598 UTC on 15 September, and remains mainly negative from 15 to 16 September, and eventually returning  
599 to positive, reflecting a continuously fluctuating process. The positive EPV in AE2 contributes to the  
600 influx of colder subsurface water into the upper layers, resulting in surface and subsurface water cooling  
601 and an increase in salinity in the subsurface (Fig. 6c-d).

602 Considering the influence of the background flow field, the pumping rate  $W$  is not only related to the  
603 wind stress curl (undisturbed Ekman pumping), but also related to the curl of background geostrophic

删除了: Compares

删除了:

删除了: causes

删除了:

删除了:

带格式的: 公式1, 缩进: 首行缩进: 0 字符, 行距: 单倍行距

设置了格式: 英语(美国)

删除了: .

设置了格式: 上标, 非突出显示

删除了: .

删除了: The EPV of

设置了格式: 上标, 非突出显示

删除了: is

删除了: the time

删除了: typhoon

删除了:

删除了: On the other hand, AE2 exhibits a more fluctuating pattern. It is positive on 14 September, has both positive and negative values at 0000 UTC on 15 September, and is mainly negative from 15 September to 16 September, and then becomes positive again, which is a constantly fluctuating process. The positive EPV in AE2 contributes to the influx of colder subsurface water into the upper layers, resulting in surface and subsurface water cooling and increases salinity in the subsurface (Fig. 6c-d). Correspondingly, the variations in Ekman layer depth ( $D_E$ ) with the typhoon's passage are similar to EPV, as shown in Fig. 10. When Kalmaegi approaches at 0000 UTC on 14 September, the mean  $D_E$  within AE1 is only 21 m, while in AE2, it is 114 m. This indicates that AE2 has already been influenced by typhoon Kalmaegi. Subsequently, the depth of the DE within AE2 sharply deepens, reaching its maximum depth of 241 m at 0000 UTC on 15 September, coinciding with the proximity of typhoon Kalmaegi's center to AE2. As Kalmaegi moves northwest, the  $D_E$  within AE1 achieves its maximum depth of 262 m at 0000 UTC on 16 September. The trends of  $D_E$  within AE1 and AE2 are nearly consistent, but AE1 lags behind AE2 by one day. Starting from 15 September,  $D_E$  within both AE1 and AE2 gradually shallows, reaching a minimum  $D_E$  of 60 m. This value is 28 m higher than before the typhoon, indicating the lingering effects of the typhoon through wind. For AE2,  $D_E$  reached its minimum of 45 m at

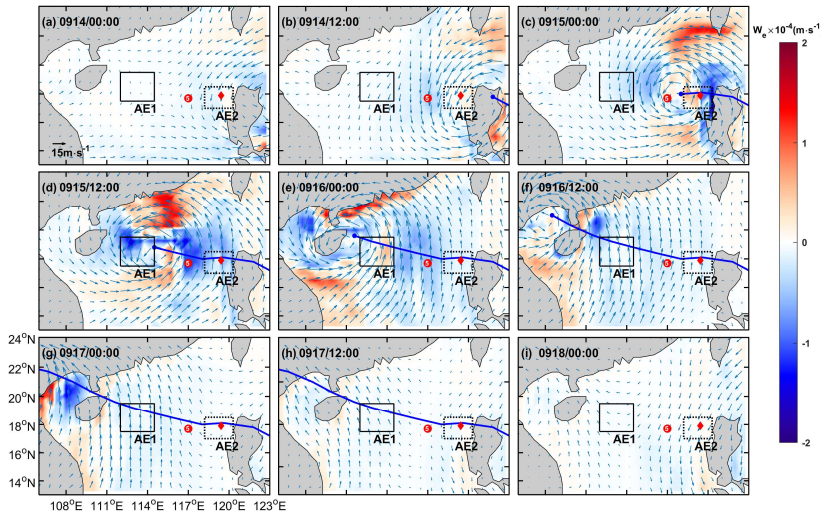
带格式的: 缩进: 首行缩进: 1 字符

664 flow (nonlinear Ekman pumping). Therefore, in order to describe the response of upwelling and  
 665 downwelling more accurately, a parametric TC-driven pumping velocity scale (Jaimes and Shay, 2015),

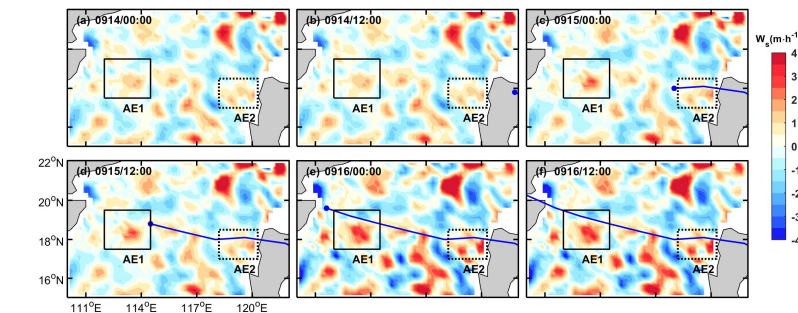
$$666 \quad W_s = W_E - R_o \delta (U_h + U_{OML}) \quad (11)$$

667 is derived from the time-dependent vorticity balance in the ocean mixed layer. Here  $W_E$  calculated  
 668 by Eq. (8),  $R_o$  is calculated using Eq. (3), the aspect ratio is calculated by  $\delta = \frac{h}{R_{max}}$ , here  $h$  represents  
 669 oceanic mixed layer thickness,  $U_h$  denotes the translation speed, and oceanic mixed layer Ekman drift  
 670 is calculated by  $U_{OML} = \frac{\tau_{Rmax}}{\rho h U_h}$ . The vertical velocity  $W_s$  calculated by Eq. (11) are presented in Figure  
 671 10. When Typhoon Kalmaegi passes through AE1, the  $W_s$  in AE1 obviously increases, while AE2  
 672 experiences minimal change.

带格式的: 公式1, 缩进: 首行缩进: 0 字符, 行距: 单倍行距



673 Figure 9. Ekman Pumping Velocity (EPV) from 14 September to 18 September (a-i). The color represents the EPV,  
 674 the blue solid line is the path of Kalmaegi, the red dot and diamond are the positions of Station 5 and Argo 2901469  
 675 on 15 September, respectively.  
 676



677 Figure 10. TC-driven pumping velocity ( $W_s$ ) from 14 September to 16 September (a-f). The color represents the  
 678  $W_s$ , the blue solid line is the path of Kalmaegi. Negative and positive values are for upwelling and downwelling  
 679 regimes, respectively.  
 680

删除了: Ekman layer depth

删除了: ( $D_E$ )

删除了:

删除了: 18

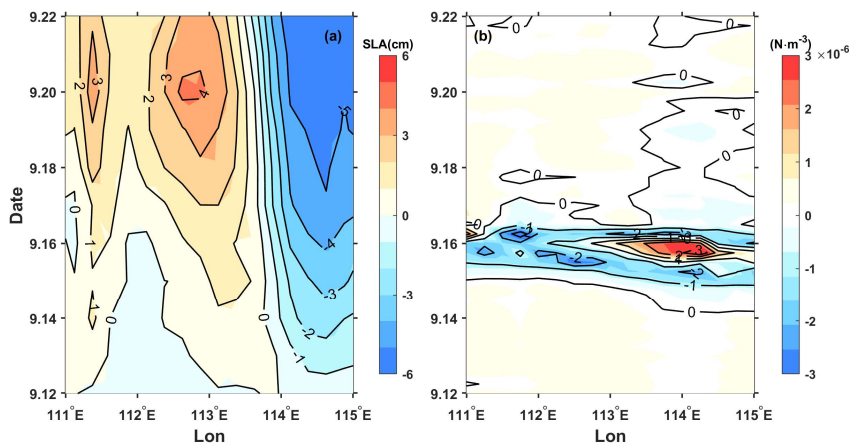
删除了: i

删除了:  $D_E$

删除了: , the red dot and diamond are the positions of Station 5 and Argo 2901469 on 15 September, respectively

设置了格式: 英语(英国)

689 Starting from 15 September, a significant positive sea level anomaly (SLA) to the west of 113.5°E  
 690 becomes evident, intensifying and reaching its maximum on 20 September (Fig. 11a). This strengthening  
 691 aligns with the increase in the amplitude of the warm core of the eddy AE1. A comparison with the wind  
 692 stress curl anomaly (Fig. 11b) reveals that between 15 to 16 September, as the Typhoon Kalmaegi moves  
 693 over the section at 18.2°N, specifically to the west of 113.5°E, it exhibits strong negative wind stress curl  
 694 anomalies, with a maximum intensity of  $-3 \times 10^{-6} \text{ N}\cdot\text{m}^{-3}$ . The combined influence of negative wind stress  
 695 curl and eddy strengthening enhances the downwelling of warm eddy and inputs negative vorticity into  
 696 AE1, leading to its intensification (Fig. 4b-c), as indicated by the enhanced positive SLA (Fig. 11a).  
 697 Conversely, the region to the east of 113.5°E along the section exhibited negative SLA anomalies. This  
 698 weakening is consistent with the previous observations of the intensified warm core and decreased eddy  
 699 area.



700  
 701 **Figure 11.** The time/longitude plots of (a) SLA anomaly (cm) and (b) wind stress curl ( $\text{N}\cdot\text{m}^{-3}$ ) anomaly at the central  
 702 section of AE1 (18.2°N). The anomalies were calculated relative to the average value of 10-13 September.

703 The response of AE2 differs from that of AE1 mainly because AE2 is quite near the Typhoon  
 704 Kalmaegi's track. As the typhoon passes through AE2, the  $R_{max}$  is 46 km. AE2 is merely 26 km away  
 705 from the typhoon center (Fig. 3). The significantly positive wind stress curl at the typhoon center induces  
 706 upwelling and positive vorticity downward into the eddy (Huang and Wang, 2022), and noticeably  
 707 weakens the eddy, corresponding to the decrease in SLA (Fig. 12a). Furthermore, based on the meridional  
 708 isotherm profiles of the eddy center at three dates, it can be observed that during the passage of Typhoon  
 709 Kalmaegi (15 September), the isotherms in the AE1 region exhibit significant subsidence (Fig. 13a),  
 710 while in the AE2 region, the isotherms show uplift (Fig. 13b). This result aligns with the earlier  
 711 observation that the convergence and subsidence within the warm eddy AE1 are enhanced by the  
 712 influence of the wind stress curl induced by the typhoon, while the intensity of AE2 is weakened.

删除了: (Jaimes and Shay, 2015) presented generated After traversing the warm ocean characteristics of AE2, Typhoon Kalmaegi becomes stronger and the maximum wind radius becomes smaller. As it passes through AE1, the maximum wind radius is measured at 35 km. Notably, the center of AE1 is located outside the maximum wind radius, approximately 104 km away from the typhoon center (Fig. 3). Hence, the hypothesis presents here suggests that the observed intensification of AE1 on the left side of the typhoon track is more likely attributed to the negative wind stress generates outside the maximum wind radius, driving the enhancement of downwelling in the pre-existing anticyclonic feature in the ocean.

删除了: .

删除了: The negative wind stress curl induces induced by the typhoon results in favourable surface ocean currents that further enhances enhances the clockwise rotation of the warm eddy. The negative wind stress curl anomaly results in strong downwelling currents, inputting negative vorticity into AE1

删除了: indicates

删除了:

删除了: .

删除了: , essentially falling within two-times the maximum wind radius of the typhoon

删除了: The response of AE2 is different from AE1 mainly because AE2 is quite near the typhoon Kalmaegi's track. When the typhoon passes through AE2, the maximum wind radius is 48km. AE2 is only 26 km away from the center of the typhoon, and its central area is basically within the maximum wind radius of the typhoon (Fig. 3). The significantly positive wind stress curl at the center of the typhoon induces upwelling and positive vorticity downward into the eddy (Huang and Wang, 2022), noticeably weakens the eddy, corresponding to the decrease in SLA (Fig. 12a)

删除了: bases

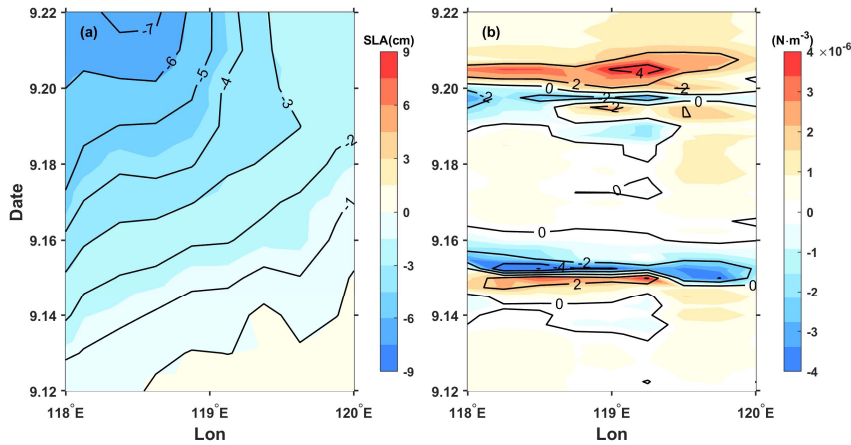
删除了:

删除了: periods

删除了: [?]

设置了格式: 非突出显示

删除了: enhances



749  
750 **Figure 12.** Same as Fig.10, but for AE2(17.9 °N).

751 From the above, the relative position of eddies and the typhoon can influence the response of the  
752 eddies (Lu et al., 2020). The warm eddy AE1, located on the left side of the typhoon track, is not  
753 weakened by the strong cold suction effect caused by the typhoon Kalmaegi. Instead, it is strengthened  
754 due to the stronger negative wind stress curl generated by the typhoon.

755 To understand the work done by the Typhoon Kalmaegi on the eddies in the ocean, we estimate the  
756 total work inputted into the ocean current  $u_c$  using the previously calculated wind stress (Liu et al.,  
757 2017):

$$758 \quad W = \int \vec{\tau} \cdot \vec{u}_c dt . \quad (12)$$

759 Here, we select the region near the typhoon track where the wind speed exceeds  $17 \text{ m s}^{-1}$  as the typhoon  
760 forcing region to know the energy input by the typhoon to the warm eddy (Sun et al., 2010). The forcing  
761 duration over the ocean in the typhoon-affected region and the work done by the typhoon on the surface  
762 current are shown in Fig. 14. When the angle between the wind and the ocean current is acute, the typhoon  
763 does positive work on the ocean current. Conversely, when the angle is obtuse, the typhoon does negative  
764 work on the ocean current. It is evident that the region with the maximum forcing duration by the typhoon  
765 on AE1 corresponds to the area where the typhoon clearly does positive work on the ocean current,  
766 accumulating a work done exceeding  $8 \text{ KJ m}^{-2}$ . This acceleration of the flow velocity in the eddy results  
767 in convergence within the eddy and an increase in SLA, leading to the strengthening of AE1. On the  
768 other hand, the forcing duration by the typhoon on AE2 is smaller, and the typhoon does negative work  
769 on the ocean current in most areas, with a cumulative work done within  $-5 \text{ KJ m}^{-2}$ , causing the flow  
770 velocity within the AE2 to decelerate.

删除了: locates

删除了: causes

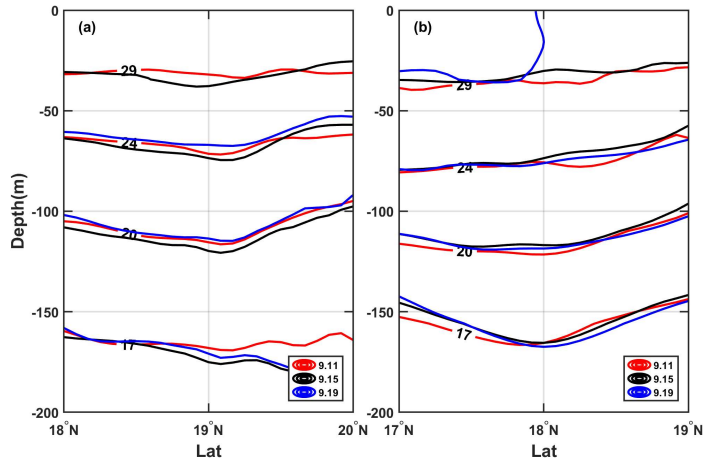
删除了: 10

删除了: .

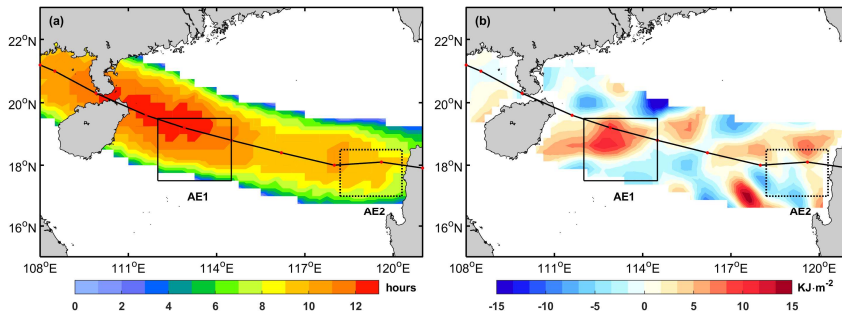
删除了: understand

删除了: [? Use a different word]

删除了: 13



778  
779 **Figure 13.** The meridional isotherm profiles of AE1 (a) and AE2 (b) before (11 September), during (15 September)  
780 and after (19 September) typhoon Kalmaegi.



782  
783 **Figure 14.** (a): the forcing time (unit: hours) of the typhoon; (b): the input work (unit:  $\text{KJ m}^{-2}$ ) of the typhoon to  
784 the current.

## 785 5. Summary

786 Based on multi-satellite observations, in situ measurements, and numerical model data, we have  
787 gained valuable insights into the response of warm eddies AE1 and AE2 in the northern South China Sea  
788 to Typhoon Kalmaegi. Both horizontally and vertically, these eddies display distinct differences.  
789 Horizontally, AE1, locates outside the  $R_{max}$  of typhoon, strengthens with amplitude,  $R_0$  and EKE after  
790 the typhoon passed. In contrast, AE2, which positions within the  $R_{max}$  of typhoon, weakens with  
791 amplitude,  $R_0$  and EKE. Vertically, during the typhoon's passage, AE1 experiences intensified  
792 converging subsidence flow at its center, leading to an increase in temperature and a decrease in salinity  
793 above 150 m. This response is more pronounced below the MLD ( $1.3^\circ\text{C}$ ) and persists for about a week  
794 after the typhoon. On the other hand, AE2 exhibits cooling above the MLD, accompanied by a decrease  
795 in salinity, as well as a subsurface temperature drop and salinity increase due to the upwelling of cold

删除了: .

删除了: on-site

删除了: we observe a reduction of areas by approximately 31% (AE1) and 36% (AE2).

删除了: positions

删除了: on

删除了: left side

删除了: the

删除了: 's track

删除了: increasing by  $1.3 \text{ cm}$ ,  $1.4 \times 10^{-2}$  and  $107.2 \text{ cm}^2 \text{ s}^{-2}$

删除了: intersects

删除了: the typhoon's track

删除了: decreasing by  $3.1 \text{ cm}$ ,  $1.6 \times 10^{-2}$  and  $38.5 \text{ cm}^2 \text{ s}^{-2}$ , respectively...

删除了: accompanies



811 water caused by the typhoon's suction effect. Additionally, it can be seen that the non-eddy region also  
812 experiences significant cooling, with a prominent cooling center observed at a depth of 60 m (-1.2 °C).

813 Further analysis reveals that the different responses of the warm eddies can be attributed to factors  
814 such as wind stress curl distribution, which are influenced by the relative position of the warm eddies  
815 and the typhoon track. The wind stress curl induced by the typhoon plays a crucial role in shaping the  
816 response of the warm eddies. AE1 locates outside the  $R_{max}$  of typhoon, is subjected to the negative wind  
817 stress curl of typhoon, which causes typhoon to input potential vorticity perturbation into the eddy.  $W_e$   
818 is enhanced by wind stress curl and quasi-geostrophic adjustment of the perturbed eddies. Therefore, the  
819 downwelling within the AE1 is obvious and contributing to its increased strength. In contrast, AE2,  
820 positioned directly below the typhoon's track, experiences shorter forcing duration and weakens due to  
821 the strong positive wind stress curl at the typhoon's center. Furthermore, the absolute value of EPV  
822 increases in both warm eddies during the typhoon's passage, but with differing impacts. Under typhoon  
823 conditions, the combined action of wind Ekman pumping and eddy-Ekman pumping makes the same  
824 polar eddies respond differently to typhoon at different positions.

825 While numerous prior studies exploring the interaction between TCs and eddies have predominantly  
826 drawn generalized conclusions, such as the weakening (strengthening) effect of cold (warm) eddies.  
827 Conversely, TCs are recognized for strengthening cold eddies and weakening warm eddies. However,  
828 our study takes a different approach. We aim to illustrate that even when TCs encounter eddies of the  
829 same polarity, the response of these eddies to TCs exhibits variations. This nuanced response is intricately  
830 linked to factors including the relative position of the eddies and the TCs, the eddies' intensity, and the  
831 background current. It is discussed first time in the South China Sea. By analyzing wind stress curl  
832 distribution, EPV, buoyancy frequency and the relative position between the eddies and the typhoon's  
833 track, this case study provides a more nuanced understanding of the mechanisms driving these different  
834 eddy-typhoon interactions in the Northern South China Sea. Moreover, it will further improve the  
835 accuracy of TC forecasts and enhancing the simulation capabilities of air-sea coupled models.

836  
837  
838 *Data availability.* The six-hourly best-track typhoon datasets were accessed on 3 February 2021 by JTWC,  
839 <http://www.usno.navy.mil/JTWC>, JMA, <https://www.jma.go.jp/jma/jma-eng/jma-center/rsmc-hp-pub-eg/besttrack.html> and CMA, <http://tcdata.typhoon.gov.cn>. The AVISO product was accessed on 14 February  
840 2021 by <https://marine.copernicus.eu/>. The AVHRR SST data was accessed on 16 March, 2022 by  
841 [ftp://podaac.jpl.nasa.gov/documents/dataset\\_docs/avhrr\\_pathfinder\\_sst.html](ftp://podaac.jpl.nasa.gov/documents/dataset_docs/avhrr_pathfinder_sst.html). The Argo data was accessed  
842 on 4 April, 2022 by <https://dataselection.euro-argo.eu/>. The wind data was accessed on 5 January, 2023 by  
843 <https://apps.ecmwf.int/datasets/data/interim-full-daily/levtype=sfc/>. The GLORYS12V1 was accessed on  
844 23 March, 2022 by <https://marine.copernicus.eu/>.

846 *Author contributions.* XYL and HZ contributed to the study conception and design. Material preparation, data  
847 collection and analysis were performed by YHH and XYL. GQH and YL contributed to the methodology. The

- 删除了: causes
- 删除了: The subsurface cooling and salinity increase in AE2 are further influenced by Typhoon Fung-wong.
- 删除了: from the temperature vertical profile of Argo and in-situ arrays, on 19 September,
- 删除了: observes
- 删除了: The warm eddy AE2, influenced by its own downwelling, exhibits enhanced mixing effects, resulting in a subsurface warm anomaly of 1.2 °C.
- 带格式的: 缩进: 首行缩进: 1 字符
- 删除了: induces
- 删除了: ,
- 删除了: locates
- 删除了: d
- 删除了: on the left side of the typhoon's path,
- 删除了: experience
- 删除了: prolonged forcing from the typhoon, resulting in positive work on the ocean current.
- 删除了: This
- 删除了: s a strong negative wind stress curl into the eddy, enhancing negative EPV and deepening  $D_E$ ,
- 删除了: so
- 删除了: positions
- 删除了: and shallower  $D_E$
- 删除了: The positive EPV contributes to surface water cooling and the influx of cooler subsurface water, while the negative EPV facilitates downwelling and intensifies the influence of the warm eddies.
- 删除了: In summary, the different responses of warm eddies to typhoons provide valuable insights into the complex interactions between the atmosphere and the ocean. Understanding these responses is crucial for accurate climate modeling and weather forecast. By investigating factors such as wind stress curl distribution, EPV, buoyancy frequency and the relative position of the eddies to the typhoon's track, researchers can gain a more precise understanding of the underlying mechanisms driving these interactions. This knowledge contributes to improved predictions and mitigation strategies for the impacts of typhoons and other extreme

897 original manuscript was prepared by XYL and YHH. All the authors contributed to the review and editing of  
898 the manuscript.

899 *Competing interests.* The contact author has declared that none of the authors has any competing interests.

900 *Disclaimer.* Publisher's note: Copernicus Publications remains neutral with regard to jurisdictional claims in  
901 published maps and institutional affiliations.

902 *Acknowledgements.* These data were collected and made freely available by JTWC, JMA, CMA, AVISO, AVHRR,  
903 Argo, ECMWF, COPERNICUS. All figures were created using MATLAB, in particular using the M\_Map toolbox  
904 (Pawlowicz, 2020). The authors thank the anonymous reviewers, whose feedback led to substantial im-  
905 provement of the resulting analyses, figures and manuscript

906 *Financial support.* This research has been supported by the National Natural Science Foundation of China  
907 (42227901), Southern Marine Science and Engineering Guangdong Laboratory (Zhuhai), grant number  
908 SML2020SP007 and SML2021SP207; the Innovation Group Project of Southern Marine Science and  
909 Engineering Guangdong Laboratory (Zhuhai), grant number 311020004 and 311022001; the National  
910 Natural Science Foundation of China, grant number 42206005; the open fund of State Key Laboratory of  
911 Satellite Ocean Environment Dynamics, Second Institute of Oceanography, MNR, grant number QNHX2309;  
912 General scientific research project of Zhejiang Provincial Department of Education, grant number  
913 Y202250609; the Open Foundation from Marine Sciences in the First-Class Subjects of Zhejiang, grant number  
914 OFMS006; State Key Laboratory of Tropical Oceanography (South China Sea Institute of Oceanology Chinese  
915 Academy of Sciences), grant number LTO2220.

916

917

918

## 919 **References**

920 Cabanes, C., Grouazel, A., von Schuckmann, K., Hamon, M., Turpin, V., Coatanoan, C., Guinehut, S.,  
921 Boone, C., Ferry, N., and Reverdin, G.: The CORA dataset: validation and diagnostics of ocean  
922 temperature and salinity in situ measurements, *Ocean Sci. Discuss.*, 9, 1273-1312, 2012.

923 Chen, G., Hou, Y., and Chu, X.: Mesoscale eddies in the South China Sea: Mean properties,  
924 spatiotemporal variability, and impact on thermohaline structure, *J. Geophys. Res.: Oceans*,  
925 116, <https://doi.org/10.1029/2010jc006716>, 2011.

926 Chen, Z., Yu, F., Chen, Z., Wang, J., Nan, F., Ren, Q., Hu, Y., Cao, A., and Zheng, T.: Downward  
927 Propagation and Trapping of Near-Inertial Waves by a Westward-Moving Anticyclonic Eddy in the  
928 Subtropical Northwestern Pacific Ocean, *J. Phys. Oceanogr.*, 53, 2105-  
929 2120, <https://doi.org/https://doi.org/10.1175/JPO-D-22-0226.1>, 2023.

930 de Boyer Montégut, C.: Mixed layer depth over the global ocean: An examination of profile data and a  
931 profile-based climatology, *J. Geophys. Res.: Oceans*, 109, <https://doi.org/10.1029/2004jc002378>, 2004.

932 Ezraty, R., Girard-Ardhuin, F., Piollé, J.-F., Kaleschke, L., and Heygster, G.: Arctic and Antarctic sea  
933 ice concentration and Arctic sea ice drift estimated from Special Sensor Microwave data, Département  
934 d’Océanographie Physique et Spatiale, IFREMER, Brest, France and University of Bremen Germany, 2,  
935 2007.

936 Huang, L., Cao, R., and Zhang, S.: Distribution and Oceanic Dynamic Mechism of Precipitation Induced  
937 by Typhoon Lekima, American Journal of Climate Change, 11, 133-  
938 154,<https://doi.org/10.4236/ajcc.2022.112007>, 2022.

939 Huang, X. and Wang, G.: Response of a Mesoscale Dipole Eddy to the Passage of a Tropical Cyclone:  
940 A Case Study Using Satellite Observations and Numerical Modeling, Remote Sens.,  
941 14,<https://doi.org/10.3390/rs14122865>, 2022.

942 Jaimes, B. and Shay, L. K.: Mixed Layer Cooling in Mesoscale Oceanic Eddies during Hurricanes  
943 Katrina and Rita, Mon. Weather Rev., 137, 4188-  
944 4207,<https://doi.org/https://doi.org/10.1175/2009MWR2849.1>, 2009.

945 Jaimes, B. and Shay, L. K.: Enhanced Wind-Driven Downwelling Flow in Warm Oceanic Eddy Features  
946 during the Intensification of Tropical Cyclone Isaac (2012): Observations and Theory, J. Phys. Oceanogr.,  
947 45, 1667-1689,<https://doi.org/10.1175/jpo-d-14-0176.1>, 2015.

948 Jullien, S., Menkès, C. E., Marchesiello, P., Jourdain, N. C., Lengaigne, M., Koch-Larrouy, A., Lefèvre,  
949 J., Vincent, E. M., and Faure, V.: Impact of tropical cyclones on the heat budget of the South Pacific  
950 Ocean, J. Phys. Oceanogr., 42, 1882-1906,<https://doi.org/10.1175/JPO-D-11-0133.1>, 2012.

951 Kessler, W. S.: The circulation of the eastern tropical Pacific: A review, Prog. Oceanogr., 69, 181-  
952 217,<https://doi.org/10.1016/j.pocan.2006.03.009>, 2006.

953 Li, Q., Sun, L., Liu, S., Xian, T., and Yan, Y.: A new mononuclear eddy identification method with  
954 simple splitting strategies, Remote Sens. Lett., 5, 65 - 72,<https://doi.org/10.1080/2150704x.2013.872814>,  
955 2014.

956 Li, X., Zhang, X., Fu, D., and Liao, S.: Strengthening effect of super typhoon Rammasun (2014) on  
957 upwelling and cold eddies in the South China Sea, J. Oceanol. Limnol., 39, 403-  
958 419,<https://doi.org/10.1007/s00343-020-9239-x>, 2021.

959 Lin, I. I., Chou, M.-D., and Wu, C.-C.: The Impact of a Warm Ocean Eddy on Typhoon Morakot (2009):  
960 A Preliminary Study from Satellite Observations and Numerical Modelling, TAO: Terrestrial,  
961 Atmospheric and Oceanic Sciences, 22,[https://doi.org/10.3319/tao.2011.08.19.01\(tm\)](https://doi.org/10.3319/tao.2011.08.19.01(tm)), 2011.

962 Lin, I. I., Wu, C.-C., Emanuel, K. A., Lee, I. H., Wu, C.-R., and Pun, I.-F.: The Interaction of  
963 Supertyphoon Maemi (2003) with a Warm Ocean Eddy, Mon. Weather Rev., 133, 2635-  
964 2649,<https://doi.org/10.1175/MWR3005.1>, 2005.

965 Liu, F. and Tang, S.: Influence of the Interaction Between Typhoons and Oceanic Mesoscale Eddies on  
966 Phytoplankton Blooms, J. Geophys. Res.: Oceans, 123, 2785-  
967 2794,<https://doi.org/10.1029/2017jc013225>, 2018.

968 Liu, S.-S., Sun, L., Wu, Q., and Yang, Y.-J.: The responses of cyclonic and anticyclonic eddies to  
969 typhoon forcing: The vertical temperature-salinity structure changes associated with the horizontal  
970 convergence/divergence, J. Geophys. Res.: Oceans, 122, 4974-  
971 4989,<https://doi.org/10.1002/2017JC012814>, 2017.

972 Lu, Z. and Shang, X.: Limited width of tropical cyclone-induced baroclinic geostrophic response, J. Phys.  
973 Oceanogr.,<https://doi.org/https://doi.org/10.1175/JPO-D-23-0096.1>, 2024.

974 Lu, Z., Wang, G., and Shang, X.: Response of a Preexisting Cyclonic Ocean Eddy to a Typhoon, J. Phys.  
975 Oceanogr., 46, 2403-2410,<https://doi.org/10.1175/jpo-d-16-0040.1>, 2016.



976 Lu, Z., Wang, G., and Shang, X.: Strength and Spatial Structure of the Perturbation Induced by a Tropical  
977 Cyclone to the Underlying Eddies, *J. Geophys. Res.: Oceans*, 125, <https://doi.org/10.1029/2020jc016097>,  
978 2020.

979 Lu, Z., Wang, G., and Shang, X.: Observable large-scale impacts of tropical cyclones on subtropical gyre,  
980 *J. Phys. Oceanogr.*, <https://doi.org/10.1175/JPO-D-22-0230.1>, 2023.

981 Ma, Z., Zhang, Z., Fei, J., and Wang, H.: Imprints of Tropical Cyclones on Structural Characteristics of  
982 Mesoscale Oceanic Eddies Over the Western North Pacific, *Geophys. Res. Lett.*,  
983 48, <https://doi.org/10.1029/2021gl092601>, 2021.

984 Ma, Z., Fei, J., Liu, L., Huang, X., and Li, Y.: An Investigation of the Influences of Mesoscale Ocean  
985 Eddies on Tropical Cyclone Intensities, *Mon. Weather Rev.*, 145, 1181-  
986 1201, <https://doi.org/10.1175/mwr-d-16-0253.1>, 2017.

987 Ning, J., Xu, Q., Zhang, H., Wang, T., and Fan, K.: Impact of Cyclonic Ocean Eddies on Upper Ocean  
988 Thermodynamic Response to Typhoon Soudelor, *Remote Sens.*, 11, <https://doi.org/10.3390/rs11080938>,  
989 2019.

990 Oey, L. Y., Ezer, T., Wang, D. P., Fan, S. J., and Yin, X. Q.: Loop Current warming by Hurricane Wilma,  
991 *Geophys. Res. Lett.*, 33, <https://doi.org/10.1029/2006gl025873>, 2006.

992 Price, J. F.: Upper Ocean Response to a Hurricane, *J. Phys. Oceanogr.*, [https://doi.org/10.1175/1520-0485\(1981\)011%3C0153:UORTAH%3E2.0.CO;2](https://doi.org/10.1175/1520-0485(1981)011%3C0153:UORTAH%3E2.0.CO;2), 1981.

994 Pujol, M.-I., Faugère, Y., Taburet, G., Dupuy, S., Pelloquin, C., Ablain, M., and Picot, N.: DUACS  
995 DT2014: the new multi-mission altimeter data set reprocessed over 20 years, *Ocean Sci.*, 12, 1067-  
996 1090, <https://doi.org/10.5194/os-12-1067-2016>, 2016.

997 Rudzin, J. E. and Chen, S.: On the dynamics of the eradication of a warm core mesoscale eddy after the  
998 passage of Hurricane Irma (2017), *Dyn. Atmos. Oceans*,  
999 100, <https://doi.org/10.1016/j.dynatmoce.2022.101334>, 2022.

1000 Shang, X.-d., Zhu, H.-b., Chen, G.-y., Xu, C., and Yang, Q.: Research on Cold Core Eddy Change and  
1001 Phytoplankton Bloom Induced by Typhoons: Case Studies in the South China Sea, *Adv. Meteorol.*, 2015,  
1002 1-19, <https://doi.org/10.1155/2015/340432>, 2015.

1003 Shay, L. K. and Jaimes, B.: Mixed Layer Cooling in Mesoscale Oceanic Eddies during Hurricanes  
1004 Katrina and Rita, *Mon. Weather Rev.*, 137, 4188-4207, <https://doi.org/10.1175/2009mwr2849.1>, 2009.

1005 Shay, L. K. and Jaimes, B.: Near-Inertial Wave Wake of Hurricanes Katrina and Rita over Mesoscale  
1006 Oceanic Eddies, *J. Phys. Oceanogr.*, 40, 1320-1337, <https://doi.org/10.1175/2010jpo4309.1>, 2010.

1007 Shay, L. K., Goni, G. J., and Black, P. G.: Effects of a Warm Oceanic Feature on Hurricane Opal, *Mon.*  
1008 *Weather Rev.*, 128, 1366-1383, [https://doi.org/10.1175/1520-0493\(2000\)128<1366:EOAWOF>2.0.CO;2](https://doi.org/10.1175/1520-0493(2000)128<1366:EOAWOF>2.0.CO;2), 2000.

1010 Song, D., Guo, L., Duan, Z., and Xiang, L.: Impact of Major Typhoons in 2016 on Sea Surface Features  
1011 in the Northwestern Pacific, *Water*, 10, <https://doi.org/10.3390/w10101326>, 2018.

1012 Sun, J., Ju, X., Zheng, Q., Wang, G., Li, L., and Xiong, X.: Numerical Study of the Response of Typhoon  
1013 Hato (2017) to Grouped Mesoscale Eddies in the Northern South China Sea, *J. Geophys. Res.: Atmos.*,  
1014 128, <https://doi.org/10.1029/2022jd037266>, 2023.

1015 Sun, L., Yang, Y., Xian, T., Lu, Z., and Fu, Y.: Strong enhancement of chlorophyll a concentration by a  
1016 weak typhoon, *Mar. Ecol. Prog. Ser.*, 404, 39-50, <https://doi.org/10.3354/meps08477>, 2010.

1017 Sun, L., Li, Y.-X., Yang, Y.-J., Wu, Q., Chen, X.-T., Li, Q.-Y., Li, Y.-B., and Xian, T.: Effects of super  
1018 typhoons on cyclonic ocean eddies in the western North Pacific: A satellite data-based evaluation

1019 between 2000 and 2008, *J. Geophys. Res.: Oceans*, 119, 5585-  
1020 5598,<https://doi.org/10.1002/2013jc009575>, 2014.

1021 Thompson, B. and Tkalich, P.: Mixed layer thermodynamics of the Southern South China Sea, *Clim.*  
1022 *Dyn.*, 43, 2061-2075,<https://doi.org/10.1007/s00382-013-2030-3>, 2014.

1023 Wada, A. and Usui, N.: Impacts of Oceanic Preexisting Conditions on Predictions of Typhoon Hai-Tang  
1024 in 2005, *Adv. Meteorol.*, 2010, 756071,<https://doi.org/10.1155/2010/756071>, 2010.

1025 Walker, N. D., Leben, R. R., and Balasubramanian, S.: Hurricane-forced upwelling and  
1026 chlorophyllaenhancement within cold-core cyclones in the Gulf of Mexico, *Geophys. Res. Lett.*, 32, n/a-  
1027 n/a,<https://doi.org/10.1029/2005gl023716>, 2005.

1028 Wang, G., Su, J., Ding, Y., and Chen, D.: Tropical cyclone genesis over the south China sea, *J. Mar.*  
1029 *Syst.*, 68, 318-326,<https://doi.org/10.1016/j.jmarsys.2006.12.002>, 2007.

1030 Wang, G., Zhao, B., Qiao, F., and Zhao, C.: Rapid intensification of Super Typhoon Haiyan: the  
1031 important role of a warm-core ocean eddy, *Ocean Dyn.*, 68, 1649-1661,<https://doi.org/10.1007/s10236->  
1032 018-1217-x, 2018.

1033 Xiu, P., Chai, F., Shi, L., Xue, H., and Chao, Y.: A census of eddy activities in the South China Sea  
1034 during 1993–2007, *J. Geophys. Res.: Oceans*, 115,<https://doi.org/10.1029/2009jc005657>, 2010.

1035 Yan, Y., Li, L., and Wang, C.: The effects of oceanic barrier layer on the upper ocean response to tropical  
1036 cyclones, *J. Geophys. Res.: Oceans*, 122, 4829-4844,<https://doi.org/10.1002/2017jc012694>, 2017.

1037 Yu, F., Yang, Q., Chen, G., and Li, Q.: The response of cyclonic eddies to typhoons based on satellite  
1038 remote sensing data for 2001–2014 from the South China Sea, *Oceanologia*, 61, 265-  
1039 275,<https://doi.org/10.1016/j.oceano.2018.11.005>, 2019.

1040 Yu, J., Lin, S., Jiang, Y., and Wang, Y.: Modulation of Typhoon-Induced Sea Surface Cooling by  
1041 Preexisting Eddies in the South China Sea, *Water*, 13,<https://doi.org/10.3390/w13050653>, 2021.

1042 Zhang, H.: Modulation of Upper Ocean Vertical Temperature Structure and Heat Content by a Fast-  
1043 Moving Tropical Cyclone, *J. Phys. Oceanogr.*, 53, 493-508,<https://doi.org/10.1175/jpo-d-22-0132.1>,  
1044 2022.

1045 Zhang, H., Chen, D., Zhou, L., Liu, X., Ding, T., and Zhou, B.: Upper ocean response to typhoon  
1046 Kalmaegi (2014), *J. Geophys. Res.: Oceans*, 121, 6520-6535,<https://doi.org/10.1002/2016jc012064>,  
1047 2016.

1048 Zhang, Y., Zhang, Z., Chen, D., Qiu, B., and Wang, W.: Strengthening of the Kuroshio current by  
1049 intensifying tropical cyclones, *Science*, 368, 988-993,<https://doi.org/10.1126/science.aax5758>, 2020.

1050

1051

第 17 页: [1] 删除了 亦豪 何 2024/1/22 21:09:00

第 22 页: [2] 删除了 亦豪 何 2024/1/22 21:12:00